Static three-dimensional topological solitons in fluid chiral ferromagnets and colloids

Paul J. Ackerman[1,2] and Ivan I. Smalyukh[1,2,3,4]★

Three-dimensional (3D) topological solitons are continuous but topologically nontrivial field configurations localized in 3D space and embedded in a uniform far-field background, that behave like particles and cannot be transformed to a uniform state through smooth deformations. Many topologically nontrivial 3D solitonic fields have been proposed. Yet, according to the Hobart–Derrick theorem, physical systems cannot host them, except for nonlinear theories with higher-order derivatives such as the Skyrme–Faddeev model. Experimental discovery of such solitons is hindered by the need for spatial imaging of the 3D fields, which is difficult in high-energy physics and cosmology. Here we experimentally realize and numerically model stationary topological solitons in a fluid chiral ferromagnet formed by colloidal dispersions of magnetic nanoplates. Such solitons have closed-loop preimages—3D regions with a single orientation of the magnetization field. We discuss localized structures with different linking of preimages quantified by topological Hopf invariants. The chirality is found to help in overcoming the constraints of the Hobart–Derrick theorem, like in two-dimensional ferromagnetic solitons, dubbed 'baby skyrmions'. Our experimental platform may lead to solitonic condensed matter phases and technological applications.

Starting from Gauss and Kelvin, knotted fields with particle-like properties have long attracted the interest of mathematicians and physicists alike[1,2]. Hopf demonstrated that three-dimensional (3D) space can be smoothly filled with inter-linked circles or torus knots[3], and Heisenberg considered such configurations in discussing the nature of countable particles in continuous fields, which could arise as 3D solitons[4]. However, according to the Hobart–Derrick theorem[5,6], such 3D solitons cannot be stable in physical systems, with the exception of nonlinear theories[7–9]. After decades of theoretical research, 3D knotted solitons—often called 'hopfions'—arise in many branches of science, including hydrodynamics, optics, cosmology, condensed matter, particle, nuclear and atomic physics[1,10–17]. However, their structure, topology and stability are rarely accessible to experimentation[10–12]. In this work, we study static 3D solitons in the magnetization and molecular alignment fields of monodomain chiral ferromagnetic liquid crystal colloids (CFLCCs) comprising magnetic nanoplates with spontaneous long-range ferromagnetic ordering in a nematic fluid host[18,19]. CFLCCs provide an advantage of hosting such solitonic structures with dimensions in the micrometre range, so that they can be probed through direct 3D optical imaging. Reconstructed experimental 3D solitonic field configurations closely agree with predictions of numerical modelling based on free energy minimization. By analysing the 3D structure of spatially localized fields, we identify and classify topological solitons with different Hopf invariants. We discuss the role of chirality in stabilizing them, as well as how CFLCCs can serve as model systems in the studies of structure, topology and dynamics of the 3D solitons. Finally, we discuss how fluid chiral ferromagnets can serve as a test bed for probing the structure and stability of topological solitons and how the experimental platform we have introduced may lead to solitonic condensed matter phases and technological applications.

Despite being merely theoretical predictions just over a decade ago[20–25], two-dimensional (2D) ferromagnetic solitons (Fig. 1a), often called 'baby skyrmions', attract a great deal of current fundamental research interest, and form a basis for skyrmionics and other emerging technologies. Embedded in a uniform far-field background, the vector field $\mathbf{m}(\mathbf{r})$ of such a magnetic skyrmion is continuous and spatially localized, but topologically nontrivial, so that it cannot be eliminated through smooth deformations[25]. Local orientations of $\mathbf{m}(\mathbf{r})$ of a ferromagnet can be uniquely described by points on a 2D unit sphere S^2 (inset of Fig. 1a). Mapping $\mathbf{m}(\mathbf{r})$ of a 2D skyrmion (Fig. 1a) fully covers S^2, consistent with the topologically protected nature of this 2D soliton[25]. To show how one can form a 3D topological soliton, the hopfion, we recall the concept of 'preimage', the spatial region of the ferromagnet's 3D space with a single $\mathbf{m}(\mathbf{r})$-orientation corresponding to a point on S^2 (Fig. 1b)[1,2]. For hopfions, preimages of all points on S^2 are closed loops, including the preimage of the north-pole point corresponding to a uniform far-field, say $\mathbf{m}_0 = (0,0,1)$, which closes into a loop through infinity (Fig. 1c). Much like in the famous mathematical Hopf fibration[1,3], the 3D space within a hopfion with finite dimensions is smoothly filled with closed loops of preimages that reside on nested tori (Fig. 1d). Since the hopfions smoothly embed into the uniform background $\mathbf{m}_0$, their solitonic $\mathbf{m}(\mathbf{r})$ in the 3D space is 'compactified' to a 3D sphere S^3 and the field topology is uniquely characterized by the $S^3 \rightarrow S^2$ maps and the homotopy group $\pi_3(S^2) = \mathbb{Z}$. The topological Hopf invariant Q of hopfions is interpreted as a linking number, because preimages of any two distinct points on S^2 are linked exactly Q times (Fig. 1c). To unambiguously identify topological solitons, we first use three-photon excitation fluorescence polarizing microscopy (3PEF-PM)[10,11] to demonstrate an excellent agreement between the experimental and computer-simulated solitonic structures (Fig. 2). We then develop an equivalent of the mathematical Hopf map (Fig. 1d) that relates the

[1]Department of Physics, University of Colorado, Boulder, Colorado 80309, USA. [2]Department of Electrical, Computer and Energy Engineering, University of Colorado, Boulder, Colorado 80309, USA. [3]Soft Materials Research Center and Materials Science and Engineering Program, University of Colorado, Boulder, Colorado 80309, USA. [4]Renewable and Sustainable Energy Institute, National Renewable Energy Laboratory and University of Colorado, Boulder, Colorado 80309, USA. *e-mail: ivan.smalyukh@colorado.edu
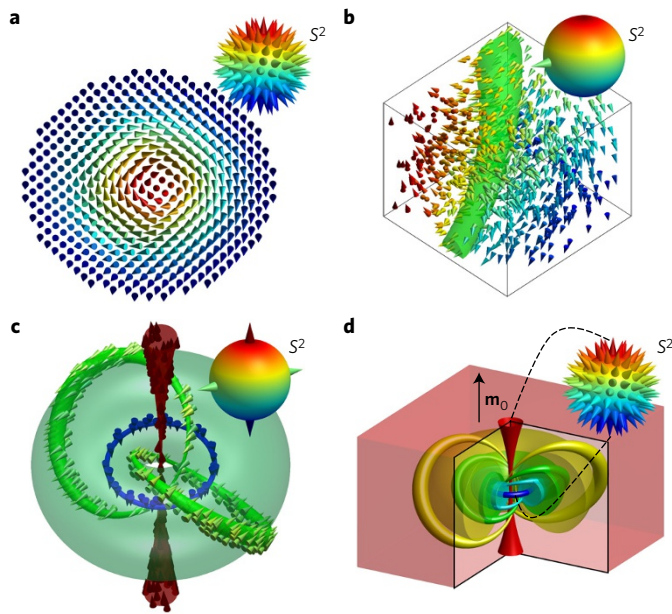
Figure 1 | 2D and 3D topological solitons. a, An example of a 2D topological soliton, called a 'baby skyrmion', with continuous $\mathbf{m}(\mathbf{r})$ twisting by π from its centre in all radial directions, as shown using cones. Mapping of $\mathbf{m}(\mathbf{r})$-orientations from the skyrmion's cross-section onto S^2 covers it once. **b**, A schematic illustrating the 'preimage' of a point on S^2 (shown using a green cone) as a 3D spatial region of the ferromagnet with the corresponding constant orientation of $\mathbf{m}(\mathbf{r})$, which we highlight by a green isosurface. **c**, Linking of the hopfion's circle-like preimages that reside on nested tori in the sample's 3D space and correspond to colour-coded points (cones) on S^2. **d**, An illustration of a Hopf map of closed-loop preimages of a 3D topological soliton embedded in a uniform far-field $\mathbf{m}_0$ onto the S^2 order parameter space of a ferromagnet.

inter-linked closed-loop preimages with all distinct points on S^2 for both experimental and theoretical 3D configurations of $\mathbf{m}(\mathbf{r})$ (Figs 3 and 4).

To be realized in chiral ferromagnets, static hopfions should emerge as local or global minima of free energy[26], which can be expressed as

$$F = \int d\mathbf{r}[A(\nabla\mathbf{m})^2 + D\mathbf{m}\cdot(\nabla\times\mathbf{m})] \quad (1)$$

where coefficients A and D describe the strengths of exchange energy and the Dzyaloshinskii–Moriya coupling[21,25,26]. For CFLCCs with intrinsic helical pitch p and $\mathbf{m}(\mathbf{r})$ describing the coupled molecular alignment and magnetization fields[19,27–31]

$$F_{\mathrm{CFLCC}} = \int d\mathbf{r} \left\{ \frac{K_{11}}{2}(\nabla\cdot\mathbf{m})^2 + \frac{K_{22}}{2}[\mathbf{m}\cdot(\nabla\times\mathbf{m})]^2 \right.$$
$$\left. + \frac{K_{33}}{2}[\mathbf{m}\times(\nabla\times\mathbf{m})]^2 + q_0 K_{22}\mathbf{m}\cdot(\nabla\times\mathbf{m}) \right\} \quad (2)$$

which reduces to equation (1) within the $K = K_{11} = K_{22} = K_{33}$ one-constant approximation for $A = K/2$, $D = Kq_0$, and $q_0 = 2\pi/p$. We note that the response of the colloidal fluid ferromagnets to strong external stimuli may require considering the finite strength of coupling between the molecular alignment and magnetization fields[29,31], but only weak or no external stimuli are used in the current work, so that $\mathbf{m}(\mathbf{r})$ describes the collinear orientation patterns of both of these fields. Numerical minimization (see Methods) of both F and F_{CFLCC} yields minima corresponding to the 3D topological solitons (Figs 3 and 4). Most of the numerical results presented

in this work are based on using equation (2) and the actual material parameters of our CFLCCs presented in Supplementary Table 1, although we find that all studied 3D solitons can be also stabilized when applying the one-elastic-constant approximation $K = (K_{11} + K_{22} + K_{33})/3$ and using equation (1). To construct preimages within such 3D solitons, we calculate a magnitude of the difference between a unit vector defining a target point on S^2 and the solitonic $\mathbf{m}(\mathbf{r})$. An isosurface of a small value in the ensuing scalar field then encloses a 3D volume of the closed-loop preimage within the CFLCC (Figs 3 and 4).

We use CFLCCs formed by long-range ordered colloidal dispersions of ferromagnetic nanoplates in a chiral nematic host (see Methods)[19], in which the unit vector field $\mathbf{m}(\mathbf{r})$ describes a spatial pattern of orientation of magnetization $\mathbf{M}$ and individual magnetic moments of nanoplates that follow the average orientation direction of rod-like nematic molecules. The confining surfaces of CFLCC samples are treated for strong perpendicular boundary conditions to align $\mathbf{m}_0 = (0,0,1)$. When sample thickness $d \approx p$, the solitons occur spontaneously, albeit their appearance can be guided by laser tweezers (Supplementary Fig. 1). 3D imaging of preimages within the solitons is based on polarized excitation through three-photon absorption and the ensuing orientation-dependent self-fluorescence of rod-like nematic molecules (Fig. 2) of the CFLCC that follow $\mathbf{m}(\mathbf{r})$, allowing us to simultaneously reconstruct pairs of preimages corresponding to the orientations $\mathbf{m}$ and $-\mathbf{m}$ (see Methods and Figs 3 and 4). To assign the individual preimages to the corresponding $\mathbf{m}$-orientations, we use the facile polar response of CFLCCs (Fig. 3c and Supplementary Figs 1–4). Polarizing optical micrographs obtained with the sample between crossed polarizers and with $\mathbf{m}_0$ along the optical axis of a microscope readily reveal CFLCC solitons and their polar response because the localized twisted $\mathbf{m}(\mathbf{r})$ departs from $\mathbf{m}_0$ and alters the polarization of light, revealing the hopfion as a bright doughnut-like feature (Fig. 3c). A magnetic field $\mathbf{B}$ applied perpendicular to the sample lateral plane and anti-parallel to $\mathbf{m}_0$ forces the soliton to grow, with outer diameter increasing and the inner region collapsing. For $\mathbf{B}$ parallel to $\mathbf{m}_0$, the soliton's outer diameter decreases and the inner diameter increases (Fig. 3c). Since the coupling of $\mathbf{B}$ and $\mathbf{M}$ is described by a free energy term $F_{\mathrm{magnetic}} = -\int d\mathbf{r}(\mathbf{B}\cdot\mathbf{M})$ added to equations (1) and (2), this observation allows removal of the $\mathbf{m}$ versus $-\mathbf{m}$ ambiguity and the determination of $\mathbf{m}_0$. Experimental preimages closely match their theoretical counterparts (Figs 3 and 4) and have shapes of closed loops that all wind around each other the same integer number of times. The topological Hopf invariant of these solitons is the linking number $Q = \Sigma C/2$ of preimages of any two distinct points on the target S^2, where the sign of crossings $C = \pm 1$ depends on the circulations of the preimages[2]. By choosing the circulation of the preimage of the north pole on S^2 to be along $\mathbf{m}_0$ through the hopfion's centre, we consistently define the circulations of all other preimages while smoothly exploring S^2. Examples of the circulations and crossings used to determine the Hopf invariant are shown in the bottom-left inset of Fig. 3a. The linking number determined for all pairs of preimages within the same soliton is conserved, yielding Q (Fig. 3 and Supplementary Movie 1). This linking cannot change without a breakdown of the $\mathbf{m}(\mathbf{r})$ continuum through melting of the CFLCC or generation of singular defects. Thus, any changes of Q require overcoming free energy barriers which, along with the medium's tendency to twist $\mathbf{m}(\mathbf{r})$, help to stabilize such topological solitons with $Q \neq 0$.

Interestingly, we find $Q = -1$ and $Q = 0$ 3D solitons in monodomain $\mathbf{m}_0 = (0,0,1)$ in the very same CFLCC sample as their $Q = 1$ counterparts (Fig. 4 and Supplementary Figs 1,5,6 and Supplementary Movies 2,3). Theoretical $\mathbf{m}(\mathbf{r})$-configurations match experiments (Figs 3 and 4) and reveal that the $Q = 0$ soliton has closed-loop preimages for a majority of points on S^2, except for the vicinity of its south pole, differing from the $Q = \pm 1$ hopfions
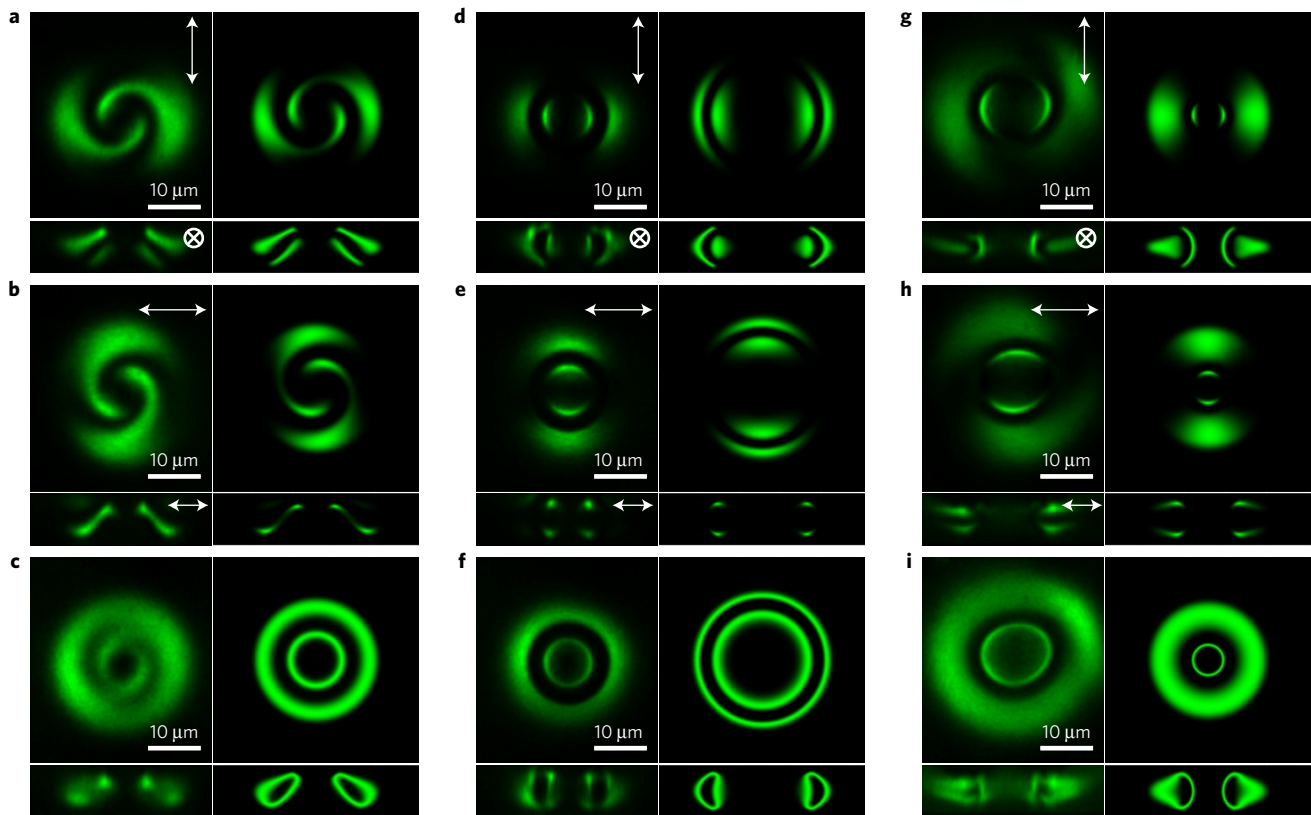
427

Figure 2 | 3D imaging of topological solitons using 3PEF-PM. a–i, Cross-sectional 3PEF-PM images of 3D solitons with $Q = 0$ (**a–c**), $Q = 1$ (**d–f**), and $Q = -1$ (**g–i**). For each panel, the images on the left were obtained experimentally and the images on the right were computer-simulated. For each panel, the top images are cross-sections orthogonal to $\mathbf{m}_0$ passing through the midplanes of the solitonic structures, whereas the bottom images are vertical cross-sections of the samples parallel to $\mathbf{m}_0$ and passing through the central axes of the 3D solitons. The polarization states of 3PEF-PM excitation light were circular for images shown in (**c,f,i**) and linear for images in (**a,b,d,e,g,h**), as marked in the top-right corners of the experimental images.

with such preimages for the entire S^2 (compare Supplementary Movies 1–3). In a magnetic field $\mathbf{B} \parallel \mathbf{m}_0$, which tends to align $\mathbf{m}(\mathbf{r})$ in the direction of the far-field background[18,19,29], the $Q = \pm 1$ solitons persist up to $\mathbf{B} \sim 3$ mT, then disappear abruptly in a complex kinetic process involving singular defects. The $Q = 0$ solitons shrink and disappear through unwinding of $\mathbf{m}(\mathbf{r})$ at lower fields < 2 mT, consistent with being homeomorphic to a uniform state. This observation suggests that although nonzero Q is not required for the stability of 3D solitons, the topology of $Q \neq 0$ solitons enhances it. Both the CFLCC and a Hopf link of any two preimages of a hopfion are chiral, so that taking a mirror image negates the linking number and Q, while also transforming a left-handed CFLCC into its right-handed counterpart, as we tested using chiral additives to induce left and right handedness (for consistency, we present all results for a left-handed CFLCC).

To further understand the stability of 3D solitons, we first recall that Hobart and Derrick demonstrated the absence of nontrivial static solitons with finite energy for Hamiltonians with only the first term in equation (1)[5,6]. Indeed, consistent with the Hobart–Derrick theorem[5,6], we numerically find no minima of free energy without including the Dzyaloshinskii–Moriya term in equations (1) and (2) (that is, for $p = \infty$). Experimentally, no 3D solitons could be found in non-chiral counterparts of CFLCCs at otherwise identical conditions. Thus, the soliton stability in confined CFLCCs benefits from embedding energetically favourable twist into the uniform unwound background of $\mathbf{m}_0$. At $d/p \approx 1$ (Fig. 5), the solitons spontaneously occur to locally relieve frustration due to the incompatibility of the perpendicular surface boundary conditions and the tendency of CFLCCs to twist $\mathbf{m}(\mathbf{r})$. For experimental parameters, the Hamiltonians given by equations (1) and (2) both yield

3D solitons with the same topology, albeit with minor structural differences and for slightly different d/p (Supplementary Fig. 7). A quantitative analysis of twist handedness[28] $\mathcal{H} = -\mathbf{n} \cdot (\nabla \times \mathbf{n})$ not only reveals how chirality tends to stabilize the twisted solitons with finite dimensions comparable to p, but also the unexpected reversal of $\mathcal{H}$ (Fig. 5a and Supplementary Figs 8,9). For example, within the $Q = 1$ hopfion, in addition to the large localized regions of twist matching the intrinsic twist handedness of the CFLCC, we also find small regions of opposite $\mathcal{H}$ (Fig. 5a) with free energy density larger than that of an unwound state (Fig. 5b). Theoretical ansatzs of hopfions used in many branches of physics exhibit reversal of $\mathcal{H}$ as well (Supplementary Fig. 10). Differing from the twisted 2D skyrmions (Fig. 1a), hopfions appear to require reversal of $\mathcal{H}$ to match their internal structure with the uniform $\mathbf{m}_0$, much like 3D packing of double twist tubes in cholesteric blue phases requires singular line defects to fill the 3D space[27].

The emergence of 3D solitons within the minimization of both equations (1) and (2) (Supplementary Fig. 7) at slightly different d/p shows that CFLCC properties can be pre-designed to enhance the hopfion stability. Although the volume fraction of ferromagnetic nanoplates in the CFLCCs studied here is low, and demagnetizing field effects are negligible, such effects may be important in concentrated dispersions[29], potentially further stabilizing topological solitons. Many-body elastic interactions between individual hopfions in the presence of a lateral confinement lead to hexagonal arrays embedded in a uniform $\mathbf{m}_0$ (Fig. 5c). The 2D hexagonal close packing of the doughnut-like north-pole preimages within the corresponding computer-simulated array (Fig. 5d) resembles that of hard-particle colloidal crystals, consistent with the particle-like nature of the topological solitons. Similar to
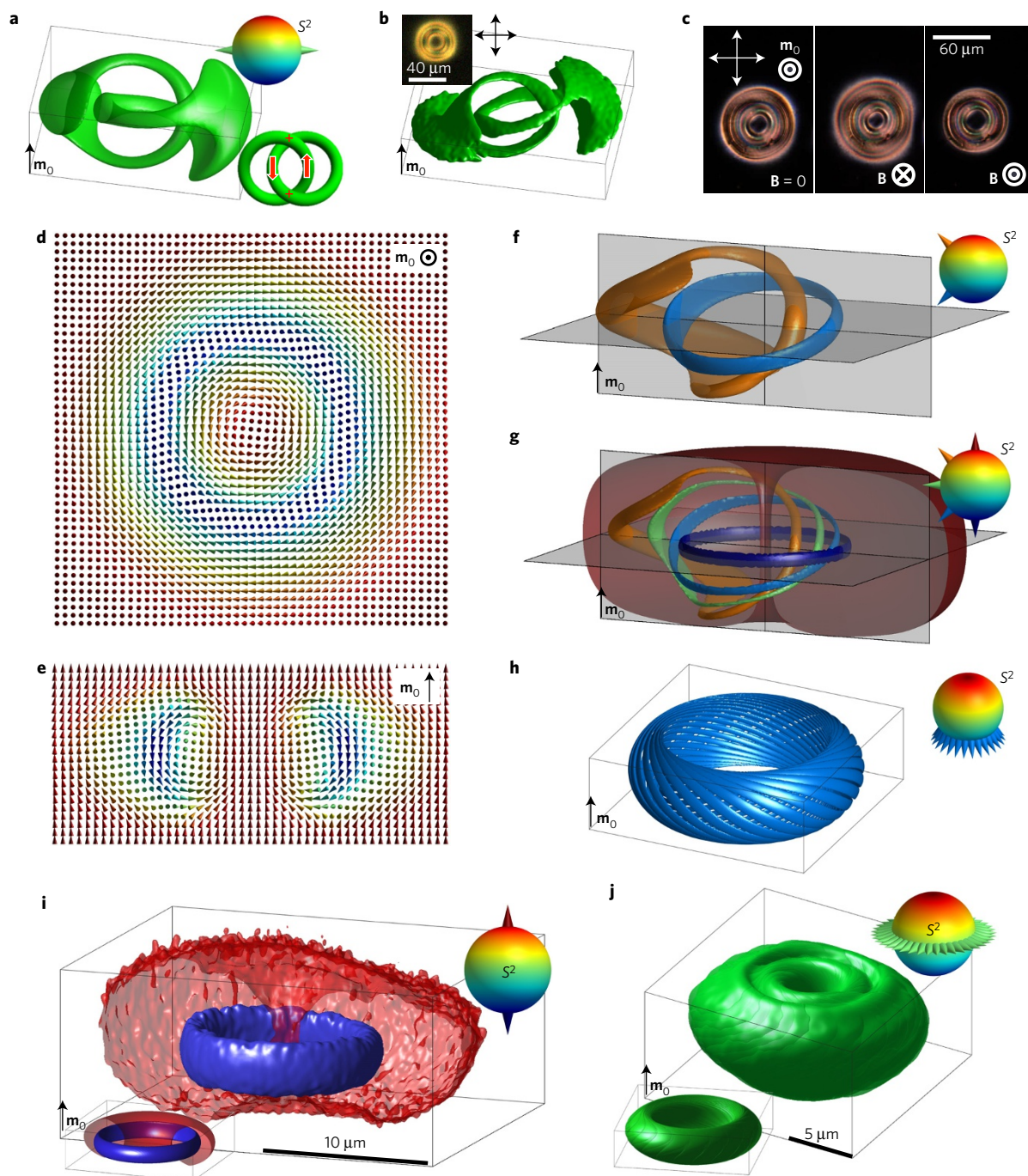
Figure 3 | Topological solitons with $Q = 1$. a,b, Computer-simulated and experimental preimages, respectively, of two diametrically opposite points on S^2 marked by cones in the top-right inset of **a**. The bottom-right inset in **a** shows signs of the crossings and circulations that determine linking of preimages. The inset in **b** is a polarizing optical micrograph of the hopfion. **c,** Polarizing optical micrographs showing the polar response of CFLCC solitons, which expand (middle micrograph) and shrink (right) as compared to their zero-field equilibrium size (left) when the magnetic field is opposite or along m_0, respectively. **d,e,** Cross-sections of the hopfion structure taken in the plane orthogonal to m_0 (**d**) and in the vertical plane parallel to m_0 (**e**), with the vector field shown using cones coloured according to the corresponding S^2 points. **f,** Linking of preimages of the two representative points on S^2. **g,** Linking of preimages of five representative points on S^2, including preimages of the south and north poles (the latter corresponds to m_0 and is shown bisected for clarity). **h,** Preimages of points on S^2 for constant polar but varying azimuthal $m(r)$-orientations that form a torus. **i,** Experimental preimages of north- and south-pole points on S^2 depicted using cones in the top-right inset, with the corresponding computer-simulated preimages shown in the bottom-left inset. **j,** Experimental preimages of 40 points on S^2 for different azimuthal orientations of in-plane $m(r)$ depicted using cones in the top-right inset; the bottom-left inset shows the corresponding 40 computer-simulated preimages tiling into a torus surface.

individual topological solitons (Fig. 3c), their arrays also exhibit a polar response to external fields (Fig. 5e,f) and can be stable even when the initially uniform background around the hopfions is switched (Fig. 5f). Such switching of CFLCCs with arrays of 3D solitons may be of interest for photonics applications. Self-assembly of hopfions may result in 2D and 3D solitonic condensed matter phases[27], analogues of the so-called 'A-phase' formed by 2D skyrmions[20–25], which calls for a detailed study of the phase diagrams
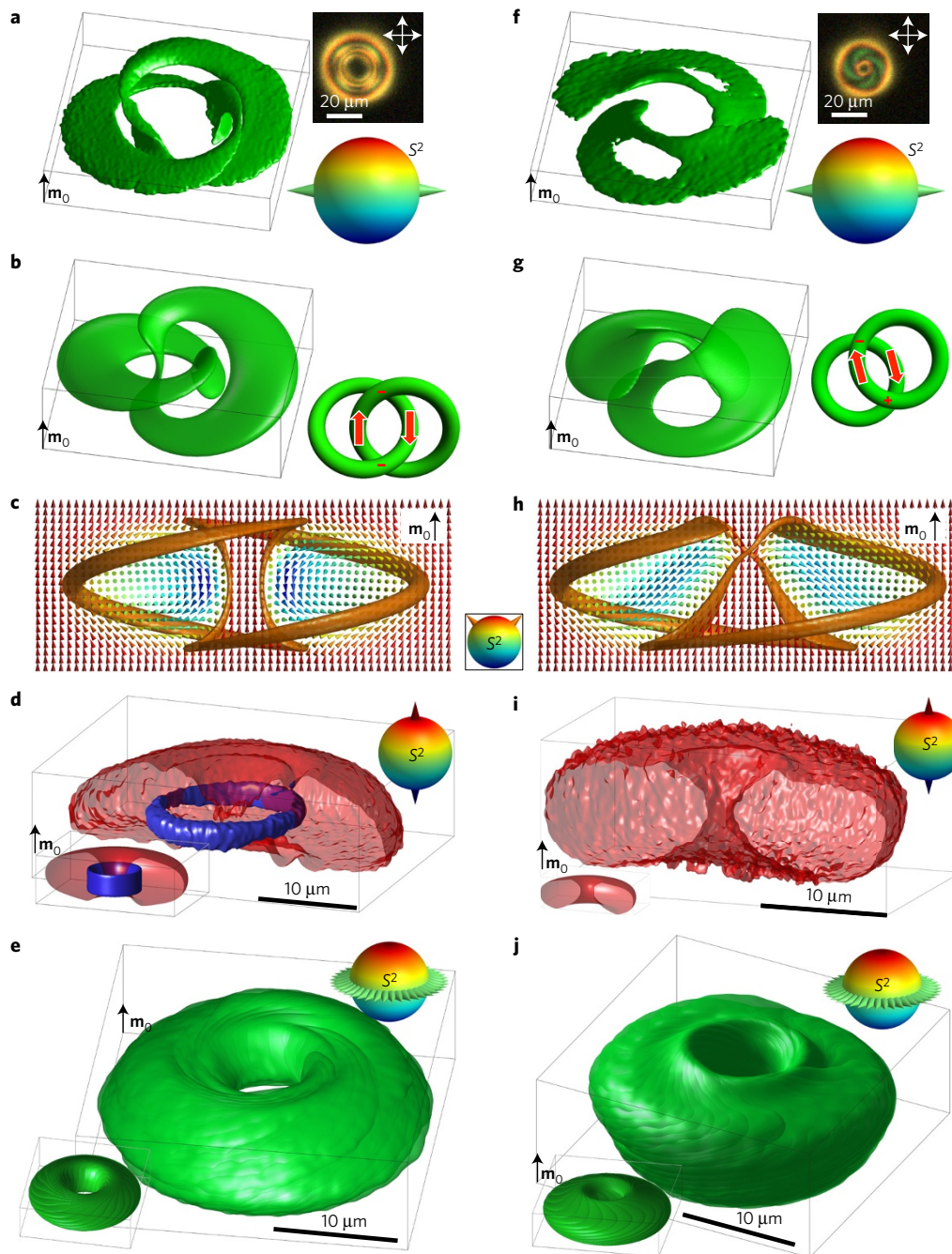
Figure 4 | Comparison of $Q = -1$ and $Q = 0$ solitons. a,b, Experimental and computer-simulated preimages, respectively, of a $Q = -1$ topological soliton for two diametrically opposite points on S^2 marked by cones in the bottom-right inset of **a**. The top-right inset of **a** shows a polarizing optical micrograph of a $Q = -1$ soliton. The bottom-right inset in **b** shows signs of the crossings and circulations that determine the linking of preimages. **c**, A vertical cross-section of the computer-simulated axially symmetric $\mathbf{m}(\mathbf{r})$-structure of the $Q = -1$ soliton shown along with the two 3D linked isosurfaces corresponding to the two representative points on S^2 (inset). **d**, Experimental preimages of north- and south-pole points on S^2 shown using cones in the top-right inset for the $Q = -1$ soliton, with the corresponding computer-simulated preimages shown in the bottom-left inset. **e**, Experimental preimages of 40 points on S^2 for different azimuthal orientations of in-plane $\mathbf{m}(\mathbf{r})$ depicted using cones in the top-right inset; the bottom-left inset shows the corresponding 40 computer-simulated preimages tiling into a torus surface for such a $Q = -1$ soliton. **f,g**, Experimental and computer-simulated preimages, respectively, of a $Q = 0$ soliton for two diametrically opposite points on S^2 (bottom-right inset). The top-right inset of **f** shows a polarizing optical micrograph of a $Q = 0$ soliton. The bottom-right inset in **g** shows signs of the crossings and circulations that reveal no linking of preimages. **h**, A vertical cross-section of the computer-simulated axially symmetric $\mathbf{m}(\mathbf{r})$ of the $Q = 0$ soliton shown along with the two 3D unlinked closed-loop isosurfaces corresponding to the two representative points on S^2 (inset). The $\mathbf{m}(\mathbf{r})$ in both **c** and **h** are shown using cones coloured according to the corresponding points on S^2. **i**, Experimental preimages of the points on S^2 shown using cones in the top-right inset, with the corresponding computer-simulated preimages of such a $Q = 0$ soliton shown in the bottom-left inset; note that there are no south-pole preimages in either the experimental or computer-simulated $\mathbf{m}(\mathbf{r})$ of this soliton, while the corresponding north-pole preimages closely match each other. **j**, Experimental preimages of 40 points on S^2 for different azimuthal orientations of in-plane $\mathbf{m}(\mathbf{r})$ depicted using cones in the top-right inset; the bottom-left inset shows the corresponding 40 computer-simulated preimages for such a $Q = 0$ soliton tiling into a torus surface.
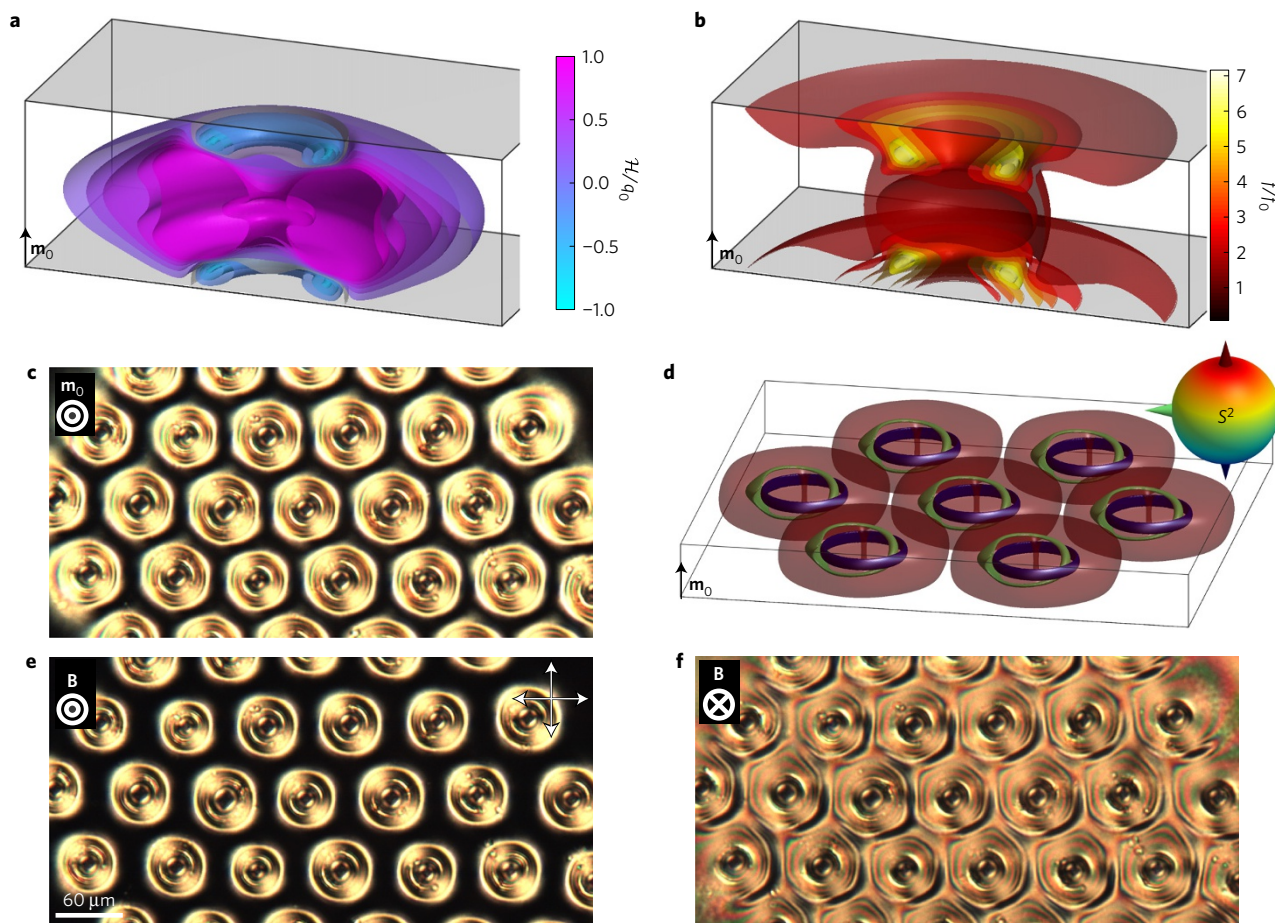
Figure 5 | Twist handedness, free energy density self-assembly and facile switching of hexagonal arrays for $Q = 1$ topological solitons. a, 3D isosurfaces depicting twist handedness $\mathcal{H}$ within the soliton, with the colour scale on the right. **b**, Isosurfaces of free energy density f within the soliton normalized by that of an unwound CFLCC ($f_0 = 2\pi^2 K_{22}/p^2$), with the colour scale on the right. The free energy density was calculated using equation (2) (without performing integration over volume $F_{CFLCC} = \int f d\mathbf{r}$) for an energy-minimizing soliton structure at $d/p = 1.2$ and parameters of 5CB-based CFLCC (Supplementary Table 1). The free energy of the array of hopfions is $\approx 2\%$ lower than that of the uniform unwound state. **c**, Polarizing optical micrograph of a 2D array of $Q = 1$ solitons. **d**, A computer-simulated array of $Q = 1$ hopfions shown using three representative preimages within a hexagonal array with lattice parameters corresponding to the experimental counterpart shown in **c**. **e,f**, Polarizing optical micrographs of a 2D array of $Q = 1$ solitons shown in **c**, but at fields ≈ 2 mT applied in the directions marked in the top-left of corresponding images.

and stability of 2D and 3D lattices of hopfions with and without additional defects, both with applied fields and without them.

The discovery of topological solitons in CFLCCs will impinge on their realization in other systems with chiral interactions, including chiral liquid crystals, non-centrosymmetric materials with spin–orbit interactions, non-centrosymmetric ferroelectrics, and gauge field theories with Chern–Simons terms, well beyond condensed matter[20]. Although all experimental and numerical studies reported above were done for CFLCCs, interestingly, minimization of the free energy given by equation (1) predicts the existence of 3D topological solitons in typical solid non-centrosymmetric ferromagnets with values of the exchange energy and Dzyaloshinskii–Moriya coupling coefficients A and D provided in Supplementary Table 1 and for thin ferromagnetic films of thickness $d \approx 4\pi A/D$. Induced anisotropy and other effects specific to different solid ferromagnets can enhance or reduce the hopfion stability and will need to be accounted for in any future detailed numerical studies of 3D solitons in solid nanolayers. Also, our modelling based on minimization of the functional given by equation (1) assumes strong perpendicular boundary conditions that define the orientation of $\mathbf{m}_0$, similar to the case of studied CFLCC samples, albeit achieving this for solid ferromagnets may require either localizing the induced anisotropy to surfaces of nanolayers of non-centrosymmetric magnets or using

other strategies. Furthermore, all hopfions discussed here, as well as several other 3D solitons, also emerge in chiral liquid crystals, and will be reported elsewhere. Since the two diametrically opposite points on the S^2 order parameter space of ferromagnets correspond to a single point on the order parameter space (RP^2) of nonpolar nematic liquid crystals, with a preimage in the form of two linked loops, a direct comparison of nematic and ferromagnetic hopfions will provide an experimental platform for probing the role of field polarity in the topology of knotted solitons.

To conclude, we experimentally realized and numerically modelled 3D solitons with different Hopf invariants in fluid chiral ferromagnets, demonstrating nonsingular localized structures with unlinked and differently linked preimages. We showed that the stability of these static solitons can be attributed to the energetically favourable twist that they introduce into a frustrated confined CFLCC system for $Q = 0$ and, additionally, to the energy barriers to change the pre-existing preimage linking required to alter the topology of $Q \neq 0$ fields. CFLCCs can serve as a test bed for experimentally probing the topology and stability of hopfions, impacting fields as diverse as particle physics and cosmology. Since only elementary $Q = \pm 1$ topological solitons have been found, our study poses a challenge of realizing hopfions with large values of the Hopf invariant, and also in solid-state chiral ferromagnets, where

they can give rise to 3D solitonic analogues of skyrmionics[24,25]. CFLCCs can also allow probing of the interplay between the nonsingular $\pi_3(S^2) = \mathbb{Z}$ solitons realized in the present study and various structures with singular defects, such as the $\pi_2(S^2) = \mathbb{Z}$ point defects that we studied recently[19]. Finally, the complex 3D patterns of orientations of anisotropic platelet-shaped colloidal nanoparticles within the topological solitons studied in this work could potentially be extended to plasmonic, semiconductor, and other kinds of nanoparticles, and thus could provide a new means of forming composite materials with unusual physical behaviour and properties.

Methods

Methods, including statements of data availability and any associated accession codes and references, are available in the online version of this paper.

References

1. Manton, N. & Sutcliffe, P. *Topological Solitons* (Cambridge Univ. Press, 2004).
2. Kauffman, L. H. *Knots and Physics* (World Scientific Publishing, 2001).
3. Hopf, H. Über die Abbildungen der dreidimensionalen Sphäre auf die Kugelfläche. *Math. Ann.* **104,** 637–665 (1931).
4. Heisenberg, W. Einführung in die einheitliche Feldtheorie der Elementarteilchen (Hirzel, 1967).
5. Derrick, G. H. Comments on nonlinear wave equations as models for elementary particles. *J. Math. Phys.* **5,** 1252–1254 (1964).
6. Hobart, R. H. On the instability of a class of unitary field models. *Proc. Phys. Soc.* **82,** 201–203 (1963).
7. Skyrme, T. H. R. A non-linear field theory. *Proc. R. Soc. A* **260,** 127–138 (1961).
8. Faddeev, L. & Niemi, A. J. Stable knot-like structures in classical field theory. *Nature* **387,** 58–61 (1997).
9. Battye, R. A. & Sutcliffe, P. M. Knots as stable soliton solutions in a three-dimensional classical field theory. *Phys. Rev. Lett.* **81,** 4798–4801 (1998).
10. Smalyukh, I. I., Lansac, Y., Clark, N. A. & Trivedi, R. P. Three-dimensional structure and multistable optical switching of triple-twisted particle-like excitations in anisotropic fluids. *Nat. Mater.* **9,** 139–145 (2010).
11. Chen, B. G., Ackerman, P. J., Alexander, G. P., Kamien, R. D. & Smalyukh, I. I. Generating the Hopf fibration experimentally in nematic liquid crystals. *Phys. Rev. Lett.* **110,** 237801 (2013).
12. Hall, D. S. *et al*. Tying quantum knots. *Nat. Phys.* **12,** 478–483 (2016).
13. Bolognesi, S. & Shifman, M. Hopf Skyrmion in QCD with adjoint quarks. *Phys. Rev. D* **75,** 065020 (2007).
14. Gorsky, A., Shifman, M. & Yung, A. Revisiting the Faddeev-Skyrme model and Hopf solitons. *Phys. Rev. D* **88,** 045026 (2013).
15. Acus, A., Norvaišas, E. & Shnir, Y. Hopfions interaction from the viewpoint of the product ansatz. *Phys. Lett. B* **733,** 15–20 (2014).
16. Thompson, A., Wickes, A., Swearngin, J. & Bouwmeester, D. Classification of electromagnetic and gravitational hopfions by algebraic type. *J. Phys. A* **48,** 205202 (2015).
17. Kobayashi, M. & Nitta, M. Torus knots as hopfions. *Phys. Lett. B* **728,** 314–318 (2014).
18. Mertelj, A., Lisjak, D., Drofenik, M. & Čopič, M. Ferromagnetism in suspensions of magnetic platelets in liquid crystal. *Nature* **504,** 237–241 (2013).
19. Zhang, Q., Ackerman, P. J., Liu, Q. & Smalyukh, I. I. Ferromagnetic switching of knotted vector fields in liquid crystal colloids. *Phys. Rev. Lett.* **115,** 097802 (2015).
20. Rößler, U. K., Bogdanov, A. N. & Pfleiderer, C. Spontaneous skyrmion ground states in magnetic metals. *Nature* **442,** 797–801 (2006).
21. Bogdanov, A. N. & Hubert, A. Thermodynamically stable magnetic vortex states in magnetic crystals. *J. Magn. Magn. Mater.* **138,** 255–269 (1994).
22. Romming, N. *et al*. Writing and deleting single magnetic skyrmions. *Science* **341,** 636–639 (2013).
23. Yu, X. Z. *et al*. Real-space observation of a two-dimensional skyrmion crystal. *Nature* **465,** 901–904 (2010).
24. Fert, A., Cros, V. & Sampaio, J. Skyrmions on the track. *Nat. Nanotech.* **8,** 152–156 (2013).
25. Nagaosa, N. & Tokura, Y. Topological properties and dynamics of magnetic skyrmions. *Nat. Nanotech.* **8,** 899–911 (2013).
26. Dzyaloshinskii, I. E. Theory of helicoidal structures in antiferromagnets. I. Nonmetals. *JETP* **19,** 960 (1964).
27. Chaikin, P. M. & Lubensky, T. C. *Principles of Condensed Matter Physics* (Cambridge Univ. Press, 2000).
28. Ackerman, P. J. & Smalyukh, I. I. Reversal of helicoidal twist handedness near point defects of confined chiral liquid crystals. *Phys. Rev. E* **93,** 052702 (2016).
29. Liu, Q., Ackerman, P. J., Lubensky, T. C. & Smalyukh, I. I. Biaxial ferromagnetic liquid crystal colloids. *Proc. Natl Acad. Sci. USA* **113,** 10479–10484 (2016).
30. Evans, J. S., Ackerman, P. J., Broer, D. J., van de Lagemaat, J. & Smalyukh, I. I. Optical generation, templating, and polymerization of three-dimensional arrays of liquid-crystal defects decorated by plasmonic nanoparticles. *Phys. Rev. E* **87,** 032503 (2013).
31. Mertelj, A., Osterman, N., Lisjak, D. & Čopič, M. Magneto-optic and converse magnetoelectric effects in a ferromagnetic liquid crystal. *Soft Matter* **10,** 9065–9072 (2014).

Author contributions

P.J.A. and I.I.S. contributed to all aspects of this work and wrote the manuscript. I.I.S. conceived and designed the project.

Additional information

Supplementary information is available in the online version of the paper. Reprints and permissions information is available online at www.nature.com/reprints. Correspondence and requests for materials should be addressed to I.I.S.

Competing financial interests

The authors declare no competing financial interests.

Methods

Preparation of CFLCCs with topological solitons. Nematic pentylcyanobiphenyl (5CB) or ZLI-2806 (both from EM Chemicals) was doped with barium hexaferrite ferromagnetic nanoplates with thickness 10 nm, diameter 195 nm, and magnetic moments $\sim 2.2 \times 10^{-17}$ Am^2 perpendicular to their large-area faces[18,19]. Strong perpendicular boundary conditions for the nematic molecules at nanoplate surfaces[19] ensure co-alignment of their orderly orientations and the dipole moments of particles along $\mathbf{m(r)}$. Left-handed chiral dopant cholesteryl pelargonate (Sigma-Aldrich) or right-handed CB-15 (EM Chemicals) was added to the dispersion at a weight fraction $C_{dopant} = 1/(h_{HTP} p)$ to define p of the ensuing CFLCC, where h_{HTP} is the separately measured helical twisting power (Supplementary Table 2)[19]. A mixture of 5CB (69%) with 12% of RM-82 and 18% of RM-257 reactive diacrylate nematics and 1% Irgacure 184 photoinitiator (CIBA Specialty Chemicals)[30] was doped with ferromagnetic nanoplates and the chiral agent to obtain partially polymerizable CFLCCs with desired value of p. Glass substrates were treated with polyimide SE1211 (Nissan Chemicals) by spin coating at 2,700 r.p.m. for 30 s and then baking (5 min at 90 °C followed by 1 h at 180 °C) to set strong perpendicular boundary conditions for $\mathbf{m(r)}$. CFLCC cells with d in the range 7–75 μm were produced using glass spacers of corresponding diameter. The hopfions occurred spontaneously after quenching the CFLCC from an isotropic phase or were generated with optical tweezers by utilizing an ytterbium-doped fibre laser (YLR-10-1064, IPG Photonics, operating at 1,064 nm) and a phase-only spatial light modulator (P512-1064, Boulder Nonlinear Systems)[30]. We laser-generated 3D solitons in a uniform unwound background $\mathbf{m_0}$ by moving the laser focus of the holographic optical trap along a circular trajectory within the cell midplane. By limiting the laser power to 50 mW, and controlling the winding direction and depth of the circular laser beam motion, we pre-selected generation of solitons with $Q=0$ and $Q=\pm 1$. The 3D solitons could also be generated more randomly upon local laser-induced heating of the CFLCC to an isotropic phase and subsequent temperature quenching.

3D nonlinear optical imaging of preimages. Imaging of $\mathbf{m(r)}$ within solitons was performed using a 3PEF-PM set-up built around a BX-81 inverted microscope (Olympus)[30]. Self-fluorescence from nematic molecules (Fig. 2) was detected in the range 400–450 nm and excited through three-photon absorption using a Ti-Sapphire oscillator (Chameleon Ultra II, Coherent) operating at 870 nm with 140 fs pulses at a repetition rate of 80 MHz. The 3PEF-PM signal was epi-detected with a photomultiplier tube (H5784-20, Hamamatsu). Beam defocusing and polarization changes due to birefringence of the CFLCC were mitigated through an order-of-magnitude reduction of the effective birefringence upon partial polymerization of the nematic host and replacement of the unpolymerized component of the system with immersion oil[30]. We used a 50× dry objective with numerical aperture NA = 0.5 and an oil-immersion 100× objective with NA = 1.4. We scanned the excitation beam through the sample volume and recorded the fluorescence signal as a function of coordinates. The linear polarization of the beam was controlled using a half-wave retardation plate to obtain multiple images with the 3PEF-PM intensity scaling as $\propto \cos^6 \beta$ (we used no polarizers in the detection channel), where β is the angle between $\mathbf{m(r)}$ and the controlled excitation beam polarization. To eliminate the ambiguity between two opposite $\mathbf{m(r)}$ tilts, additional cross-sectional images were obtained at orientations of the cell normal tilted by $\pm 2°$ with respect to the microscope axis for linear polarizations of excitation laser light parallel or perpendicular to the plane of a corresponding 3PEF-PM vertical cross-section. The $\mathbf{m(r)}$ tilt ambiguity was eliminated based on $\propto \cos^6 \beta$ scaling and the spatial changes of the 3PEF-PM signal corresponding to the $\pm 2°$ tilts. To further narrow the angular sector of $\mathbf{m}$-orientations corresponding to preimages of points on S^2 with target azimuthal angles ϕ, we obtained 3D images with azimuthal orientation of the linear polarization of excitation beam at φ and $\varphi \pm 3°$. These 3PEF-PM images were first smoothed and then used in a differential analysis to improve orientational resolution to better than $\pm 3°$. Polarized 3D imaging yields two preimages at once, due to the nonpolar nature of ordering of nematic molecules within the CFLCC, corresponding to diametrically opposite points on S^2. The preimages were then assigned to orientations $\mathbf{m}$ or $-\mathbf{m}$ based on the polar magnetic response (Fig. 3c) and continuity of $\mathbf{m(r)}$ within the 3D solitons.

Numerical modelling of solitons and preimages. Theoretical $\mathbf{m(r)}$-structures were obtained through numerical minimization of equations (1) and (2) using experimental material parameters (Supplementary Table 1). The numerical relaxation method utilized large 3D grids[19] and both analytical ansatzs[32] (Supplementary Fig. 10) and random $\mathbf{m(r)}$ mimicking a disordered phase to define

the initial conditions. The structures corresponding to free energy minima were used to generate preimages of points on S^2. The angular sectors of $\mathbf{m(r)}$-orientations corresponding to preimages derived from the theoretical free-energy-minimizing solitons were chosen to be comparable to their counterparts in preimages reconstructed from experiments.

Computer simulations of the minimum-energy (including local and global minima) $\mathbf{m(r)}$-configurations were performed using a relaxation routine. We assume that the coupling between the nematic director $\mathbf{n}$ (average molecular orientation direction) and the magnetization field $\mathbf{M(r)}$ described by a unit vector $\mathbf{m(r)}$ and given by a free energy term $F_{coupl} = -1/2 \int \gamma \mu_0 (\mathbf{n} \cdot \mathbf{m})^2 dV$ is infinitely strong, which is appropriate because of the large coupling coefficient γ [19,31]. We also assume that the surface anchoring free energy term $F_{surf} = -1/2 \int W(\mathbf{m} \cdot \mathbf{n_s})^2 ds$ ensures strong homeotropic boundary conditions and alignment of $\mathbf{m(r)}$ at the confining surfaces along the surface normal $\mathbf{n_s}$ because of the large surface anchoring energy coefficient W, so that the surface free energy does not need to be included in the free energy minimization problem[10,19,33]. Disregarding higher-order diamagnetic coupling terms, we supplement the free energy of the CFLCC system given by equations (1) and (2) of the main text with the magnetic field coupling term[19] in the form $F_{magnetic} = -\int d\mathbf{r}(\mathbf{B} \cdot \mathbf{M})$ and minimize it to obtain different 3D solitonic structures of $\mathbf{m(r)}$[19]. In numerical modelling, the Frank elastic constants K_{11}, K_{22} and K_{33}, which describe the energetic cost of splay, twist and bend deformations, respectively, are based on literature data for the two nematic hosts used (Supplementary Table 1). The magnetization $\mathbf{M}$ is dependent on the concentration of nanoplates and is adjusted in the calculations, along with the cell thickness to pitch ratio d/p, to match experimental conditions. Our numerical relaxation routine obtains spatial derivatives of $\mathbf{m(r)}$ on a computational grid using a second-order finite difference scheme. Typically, periodic boundaries are implemented along lateral directions, while fixed homeotropic boundary conditions are applied at substrate surfaces to define the far-field $\mathbf{m_0} = (0,0,1)$. In some of the simulations, the vertical conditions $\mathbf{m_0} = (0,0,1)$ were also enforced at the lateral edges of the 3D simulation box (Supplementary Fig. 3c). At each time step Δt, the functional derivatives given by the Lagrange equation $\delta F/\delta m_i = 0$ and the resulting elementary displacement $\delta m_i = -\Delta t(\delta F)/(\delta m_i)$ were computed, where the subscript i denotes orientations along the x, y, and z axes[10,19,33]. The maximum stable time step used in the relaxation routine is determined as $\Delta t = (\min(h_i)^2)/(2 \max(K))$, where $\min(h_i)$ is the smallest computational grid spacing and $\max(K)$ is the largest (or average in the case of the one-constant approximation) elastic constant. The steady-state stopping condition is determined by monitoring the change with respect to time of the spatially averaged functional derivative. When this value asymptotically approaches zero, the system is assumed to be in equilibrium and relaxation is complete. Topologically, the same structures were obtained when starting minimization from initial conditions in the form of a random $\mathbf{m(r)}$, and also from the analytical ansatz of the hopfion field configurations (Supplementary Fig. 10) taken from literature[32].

The 3D spatial discretization is performed on fairly large grids, such as the $112 \times 112 \times 32$ grid, which is important to ensure that the minimum-energy $\mathbf{m(r)}$ is indeed a localized structure in equilibrium with the surrounding untwisted CFLCC and that the periodic boundary conditions do not introduce artefacts influencing its stability. Using the grid spacing of $h_x = h_y = h_z = 1$ μm and 32 grid points across the cell implies an effective sample thickness $d = 32$ μm, comparable to that used in experiments. To speed up the relaxation of field configurations to local or global energy minima, the minimization was also performed with a relaxation method for a 2D grid of equally spaced points that was rotated to obtain a volume of equally spaced voxels on a 3D grid. Grid spacing in this case was equal in all directions and discretized into $192 \times 192 \times 64$ points in the x, y and z directions, respectively. The free-energy-minimizing computer-simulated field configurations obtained using different grids and discretization approaches were analysed and compared to each other and to experiments with the generation of 3D isosurfaces, showing that the structures we obtain are independent of the type of grid discretization.

Data availability. All relevant data are available from the authors.

References

32. Hietarinta, J. & Salo, P. Faddeev-Hopf knots: dynamics of linked un-knots. *Phys. Lett. B* **451**, 60–67 (1999).
33. Ackerman, P. J., van de Lagemaat, J. & Smalyukh, I. I. Self-assembly and electrostriction of arrays and chains of hopfion particles in chiral liquid crystals. *Nat. Commun.* **6**, 6012 (2015).